drastic variations in elevations of left and right rim of the crater (Figure 11).

It can be concluded that depth–diameter ratios of floor-fractured and degraded craters are less than fresh craters. It was also found that these ratios for fresh craters are consistent with Pike's relation. Therefore, a primary decision can be to evaluate *d*/*D*, and compare it with Pike's relation. If the ratio is low, the crater can be categorized as belonging to either floor-fractured or degraded class. The rim degradation parameters can then be used to provide the next level of discrimination. Currently, the empirical values have been decided based on analysis of these 12 craters (Table 2). Values of parameters for selected craters only and are as follows: $R_e = 0.06$, $R_r = 0.04$, $S_2 = 0.10$, $S_3 = 0.10$. Figure 12 depicts the decision tree framework based on this analysis.

Thus, an automatic classification framework to classify craters according to their post-impact modification states is proposed in this study. We can conclude that parameters depth-to-diameter ratio of the craters, elongation and lumpiness and variance of elevations of crater boundary and variance of radius in different directions are good separators among the crater three classes. Our program could automatically derive the discriminative parameters accurately and rapidly. A decision tree framework based on empirical values of parameters has been proposed. The empirical values are based on the present observations only. Our future work would focus on testing the programs on a greater number of craters and obtain more generic values of discriminative parameters.

1. Salamuničcar, G. and Lončarić, S., Open framework for objective evaluation of crater detection algorithms with first test-field subsystem based on MOLA data. *Adv. Sp. Res.*, 2008, **42**(1), 6–19.
2. Gandhi, S. and Suchit, P., Automatic crater detection techniques: a chronological survey. *Int. J. Res. Comput. Sci. Inf*, 2013, **2**(2(A)), 207–213.
3. Pike, R. J., Crater dimensions from Apollo data and supplemental sources. *Earth. Moon. Planets*, 1976, **15**(3), 463–477.
4. Head, J. W., Processes of lunar crater degradation: Changes in style with geologic time. The *Moon*, 1975, **12**(3), 299–329.
5. Schultz, P. H., Floor-fractured lunar craters. *Earth. Moon. Planets*, 1976, **15**(3), 241–273.
6. Jozwiak, L. M., Head, J. W., Zuber, M. T., Smith, D. E. and Neumann, G. A., Lunar floor-fractured craters: Classification, distribution, origin and implications for magmatism and shallow crustal structure. *J. Geophys. Res. E Planets*, 2012, **117**(11).
7. Li, B., Ling, Z. C., Zhang, J., Wu, Z. C., Ni, Y. H. and Chen, J., The shape and elevation analysis of lunar crater's true margin. In Lunar and Planetary Science Conference, Texas, 2015, vol. 46, p. 1709.
8. Losiak, A., Kohout, K., Sullivan, K. O., Thaisen, K. and Weider, S. , Lunar impact crater database. Lunar Explor. Summer Intern Progr. Lunar Planet. Inst., Texas, 2008.
9. Purohit, S., Gandhi, S. R. and Prakash, C., A novel framework for automatic determination of morphometric parameters of lunar floor-fractured craters. *Planet. Space Sci.*, 2018.
10. Smith, D. E. *et al.*, The lunar orbiter laser altimeter investigation on the lunar reconnaissance orbiter mission. *Space Sci. Rev.*, 2010, **150**(1–4), 209–241.
11. Melosh, H. J., Impact cratering: A geologic process. Oxford Univ. Press (Oxford Monogr. Geol. Geophys. No. 11), 1989, vol. 11, p. 253.
12. Oberbeck, V. R. and Quaide, W. L., Genetic implications of Lunar regolith thickness variations. *Icarus*, 1968, **9**(1–3), 446–465.
13. Stoffler, D., Cratering history and lunar chronology. *Rev. Mineral. Geochem.*, 2006, **60**(1), 519–596.
14. Chen, M., Lei, M., Liu, D., Zhou, Y., Zhao, H. and Qian, K., Morphological features-based descriptive index system for lunar impact craters. *ISPRS Int. J. Geo-Information*, 2017, 7(2), 5.
15. Baldwin, R. B., *The Face of the Moon*, University of Chicago Press, Chicago, 1949.
16. Fielder, G., *Lunar Geology*, Lutterworth Press, London, 1965.
17. Wood, C. A. and Anderson, L., New morphometric data for fresh lunar craters. In Lunar and Planetary Science Conference Proceedings, 1978, vol. 9, pp. 3669–3689.

ACKNOWLEDGEMENTS. We thank the Indian Space Research Organisation (ISRO) for financial support under the grant ISRO/SSPO/Ch-1/2016-17. We also thank Space Applications Centre, ISRO, Ahmedabad for providing expertise, technical and logistical support throughout this study.

Received 21 February 2018; revised accepted 30 June 2018

doi: 10.18520/cs/v115/i7/1351-1358

Identification of weather events from INSAT-3D RGB scheme using RAPID tool

A. K. Mitra[1], Shailesh Parihar[1], R. Bhatla[2] and K. J. Ramesh[1]

[1]National Satellite Meteorological Centre,
India Meteorological Department, New Delhi 110 003, India
[2]Banaras Hindu University, Varanasi 221 005, India

Real-time analysis of products and information dissemination (RAPID), a web-based quick visualization and analysis tool for INSAT satellite data has been presented for identification of weather events. The combination of channels using red–green–blue (RGB) composites of INSAT-3D satellite and its physical significant value content is presented. The solar reflectance and brightness temperatures are the major components of this scheme. The shortwave thermal infrared (1.6 μm), visible (0.5 μm) and thermal IR channels (10.8 μm) representing cloud microstructure is known as Day Microphysics (DMP) and the brightness temperature (BT) differences between 10.8, 12.0 and 3.9 μm is referred to as Night Microphysics (NMP). The thresholds technique have been developed

*For correspondence. (e-mail: ashim_mitra@rediffmail.com)

separately for both the RGB products of two years (2015–17 of December to February) of data for the identification of fog, snow and low clouds. The validation of these thresholds has been carried out against *in situ* visibility data from IMD observatories. The RGBs, i.e. DMP and NMP have a reasonable good agreement with ground-based observations and Moderate Resolution Imaging Spectroradiometer (MODIS) data. This threshold technique yields a very good probability of fog detection more than 94% and 85% with acceptable false alarm conditions less than 8% and 10% for DMP and NMP respectively. The technique has significantly minimized the misclassification between low clouds, snow, and fog and found useful for day-to-day weather forecast.

Keywords: INSAT-3D, RAPID, DMP, NMP, RGB.

FOG is a meteorological phenomenon causing significant societal and monetary issues, particularly to the aviation as well as transportation system especially over the northern northwestern part of India. It has also great impact in the field of meteorology, climate studies as well as on human health and crops. Thus, an enhanced comprehension observing, monitoring, forecasting and nowcasting of fog will positively benefit the society as a whole[1]. The winter season fog occurs for a considerable period over northern India[2,3]. Fog forms basically due to radiative cooling of the earth's surface during winter season, when a series of low and high-pressure zones move from NW to NE along the Himalaya. In this low-pressure zone, more moisture is added to the atmosphere due to rainfall. The current operational NWP models are incapable of simulating the progression of fog due to its dependency on mesoscale and synoptic scale processes that act with boundary layer that is influenced by the prevailing synoptic regime[4]. Extensive studies have been carried out on such weather system regarding fog formation mostly over airports[2,4–6]. In the present scenario, effect of winter fog in the North Indian region is addressed by any methods of threshold criteria in both spatial and temporal resolution. With the advancement in the field of remote sensing, it is desirable to evolve a technique that can provide better problem-solving schemes. Therefore, satellite-based fog monitoring has become popular due to its enhanced spatial, spectral and temporal resolution and offers new opportunities for near real-time fog detection and monitoring. The INSAT-3D indigenous satellite launched on 26 July 2013 has six-channels imager to provide imaging capability of the earth's disc from geostationary altitude in one visible (0.52–0.77 μm) and five infrared (IR) channels; 1.55–1.70 μm (SWIR), 3.80–4.00 μm (MIR), 6.50–7.10 μm (water vapour), 10.3–11.3 μm (TIR-1) and 11.5–12.5 μm (TIR-2) bands. The ground resolution at the sub-satellite point is nominally 1 km × 1 km for visible and SWIR bands, 4 km × 4 km for one MIR and both TIR bands and 8 km × 8 km for WV band. Recently, an on-line INSAT-3D visualization tool, RAPID has been developed by the Space Applications Center (SAC), Indian Space Research Organization (ISRO), Ahmedabad, in consultation with the India Meteorological Department (IMD), New Delhi (http://rapid.imd.gov.in; Figure 1). The RAPID provides features of interest to the scientific community with no specific operating system/software/library/compiler required on the desktop. It can run on any machine and can be accessed using any browser. It has all the features from overlaying map boundaries (world coastline, state, district boundaries and gridlines) to probing the digital INSAT-3D data on the fly in real time. On the spot computation of time-series, vertical profile, transect, area measurement and distance measurement over the pixel can also be done.

RGBs with multispectral channels are false colour images designed to enhance a specific feature such as fog, snow, dust, etc. These images are created by combining band or band differences into each of the red, green, and blue components with a defined recipe. The advantage of RGB products is the ability to look at a single image to identify a feature instead of analysing multiple single channels. In the INSAT-3D RGB, the image manipulations refer to reflectance factor (RF) values for solar channels and equivalent brightness temperature (EBT) values for IR channels. The enhancement operations expand to the full range of display values (0–1023) and a limited range (MIN, MAX) of RF or EBT values, applying subsequently a gamma correction for possible non-linear expansion[7]

$$\text{INSAT-3D}_{\text{R,G,B}} = 1023 * \left[\frac{(\text{BT}, \Delta\text{BT}, R, \Delta R) - \text{MIN}}{\text{MAX} - \text{MIN}} \right]^{(1/\gamma)},$$

where BT is the brightness temperature, ΔBT the brightness temperature difference, R the reflectance, ΔR the reflectance difference and γ is the gamma enhancement.

The minimum/maximum thresholds and gamma stretching are used to enhance the colour of features of a particular phenomenon. Most RGB images (EUMETSAT, GOES, JMA) have $\gamma = 1$, i.e. there is linear spreading of values and constant contrast between the minimum/maximum. The reflectance of solar channel and BT of INSAT-3D thermal channels are key ingredients for the preparation of the daytime and night-time microphysical products. In this study, the technique of Lensky and Rosenfeld[8] (operational in EUMESAT) has been fine-tuned according to INSAT-3D multispectral channel specifications and implemented to INSAT Meteorological Data Processing System (IMDPS) at IMD. Here fine-tuning is basically the adjustment of EUMETSAT RGB recipes to retain legacy colouring due to differing spectral characteristics between SEVIRI and INSAT-3D channels. The technique uses a meaningful RGB combination for a

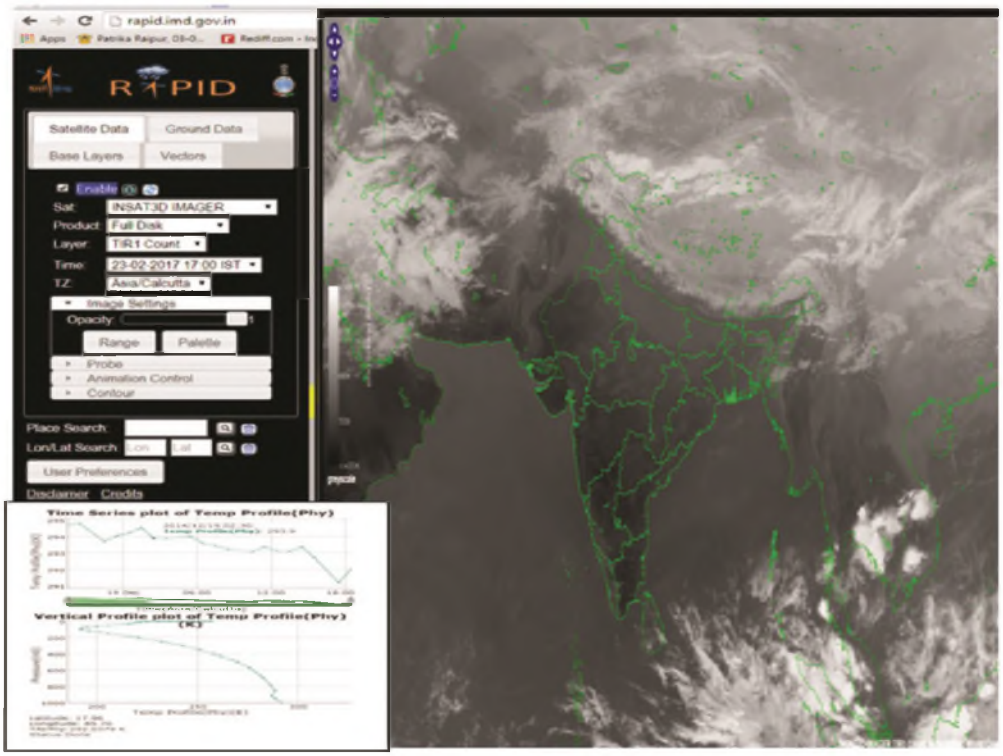

Figure 1. Rapid on IMD website.

Table 1. An RGB composition of the DMP colour scheme

Beam	Channel	Range	Gamma
Red	VIS (0.55–0.75 μm)	0… +100%	1.0
Green	SWIR (1.67 μm)	0… +60%	1.0
Blue	IR (10.8 μm)	+203… +323 K	1.0

qualitative as well as quantitative analysis of the cloud microphysics of INSAT-3D imager channels. The DMP RGB utilizes the solar reflectance of the SWIR (1.6 μm), visible (0.5 μm) and thermal IR channels (10.8 μm), whereas BT difference between (12.0–10.8 μm) and (10.8–3.9 μm) also used in the NMP RGB.

Table 1 shows an RGB composition of the DMP colour scheme along with spectral signature of 0.5, 1.6 and 10.8 μm in the RGB beams. In this RGB scheme, snow and ice clouds appear red because they strongly absorb in 1.6 μm. The small particles of ice cloud signature appear orange (western disturbance), whereas the large particles of ice cloud (Mature Cumulonimbus (CB) cell) appear with greater red component. Snow grains are larger than cloud ice particles and over the ground, they appear as full red colour. Generally, ice particles that form by mixed phase process in a supercooled water cloud grow quickly to a much larger size than crystals formed by vapour deposition in ice-only clouds. This helps to separate convective precipitating clouds from non-precipitating or layer ice clouds[8]. Because of the larger reflectance in 1.6 and 0.5 μm, deserts (dust) appear bright cyan. Ocean appears dark blue because of high-thermal emission. Figure 2 *a* shows an ideal case of the DMP colours scheme along with its physical values on 27 May 2016, 0400 UTC using RAPID. From the figure, the low/medium/CB clouds and snow can be easily demarcated. The physical values of visible albedo for low/medium/CB clouds are almost same, i.e. approximately 50% but SWIR albedo is different. For the case of snow, the albedo is low compared to low/medium/CB clouds. This is because of strong absorption in 1.6 μm. For mature CB cell, the pixel temperature is low due to the large particle of ice clouds and its value appears less than 220 K compared with higher temperatures of low/medium clouds and snow (above 250 K).

Table 2 shows an RGB composition of the NMP colour scheme along with the spectral signature of BT differences between TIR2–TIR1, TIR1–MIR and TIR1 in the RGB beams respectively. NMP is designed and tuned to monitor the evolution of night-time fog/low stratus. Other (secondary) applications are the detection of fires, low-level moisture boundaries and cloud classification. In this RGB colour scheme, BT difference between the 12.0 and 10.8 μm channels (12.0–10.8 μm) is a measure of opaqueness[9] of the clouds and is displayed in red, whereas the BT difference between 10.8 and 3.9 μm channels (10.8–3.9 μm) modulates the green beam. The BT

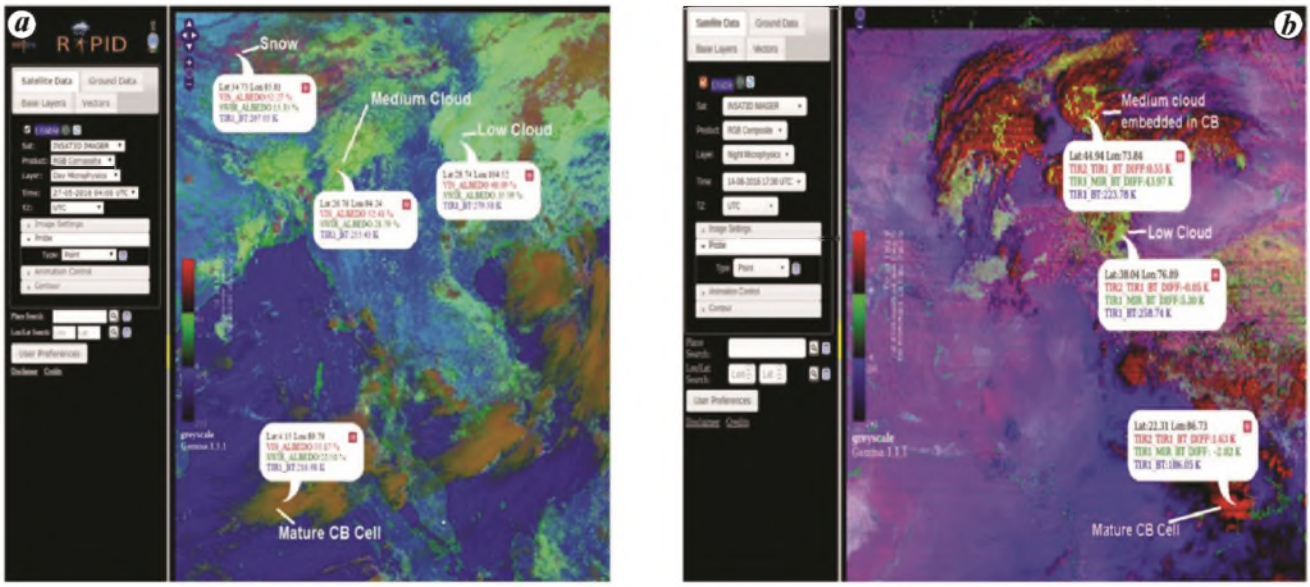

Figure 2. INSAT-3D RGB composition of the (*a*) DMP colour scheme along with its physical values on 27 May 2016, 0400 UTC and (*b*) NMP colour scheme along with its physical values on 14 June 2016, 1730 UTC.

Table 2. RGB composition of the NMP colour scheme

Beam	Channel	Range	Gamma
Red	IR 12.0–IR 10.0 um (TIR2–TIR1)	–4…+2 K	1.0
Green	IR 10.8–IR 3.9 um (TIR1–MIR)	–4…+6 K	1.0
Blue	IR 10.8 (TIR1)	+243…+293 K	1.0

difference in these two bands distinguishes stratus clouds consisting of water droplets versus cirrus clouds as well as cloud-free regions. Lensky and Rosenfeld[10] showed how sensitive is the BT difference between 10.8 and 3.9 μm channels to affects particle size, and used this information to delineate precipitation[11]. The large difference between these two channels will indicate clouds with small drops. In NMP colour scheme, fog with small drops or shallow clouds appears in white. Figure 2 *b* shows an ideal case of NMP colour scheme along with its physical values on 14 June 2016, 1730 UTC using RAPID. From the figure, the low/medium and CB clouds during night-time can be easily demarcated. The radiation emitted from the top of cold CB in 10.8 μm is very low, resulting in low temperature (<220 K) and sprinkled colour at the mature CB cell tops. Therefore, mature CB clouds at night appear in sprinkled orange–red colour compared to low and medium clouds.

The radiation difference between cloud and fog is due to the differences in spectral response which provide the basis of fog detection. Due to the limitation of single IR (10.8 μm) channel during fog, there is poor discrimination of low clouds/fog/stratus[12,13]. Therefore, to identify the extent of fog (horizontal) during night, differences in the radiative properties of fog and stratus in the 3.9 and 11 μm channels result in temperature contrasts that will allow discriminating the fog. This technique is based on the principle that the emissivity of water cloud at 3.9 μm is less than at 10.7 μm (refs 14–16). In the thermal IR, higher the temperature, greater will be the radiation from the surface, and fog will have higher temperature compared to medium and high-level clouds. Thus BT of fog will also be higher than that of medium and high clouds. Therefore, long-wave IR channel can be used to eliminate medium and high clouds, whereas it is difficult to differentiate between fog and the underlying surface using thermal channel alone[17]. For SWIR and visible channels, the albedo will be higher for fog and low clouds.

To determine the threshold criteria for identification of fog and low clouds in the RGB of DMP and NMP, the composition of channels along with their physical values have been studied and analysed from two years (2015–16 and 2016–17 of December to February) of INSAT-3D data. All the foggy days, low clouds and clear-sky conditions have been validated with actual IMD observations. Figure 3 shows the scatter plot of both the microphysics. From the figure, fog pixels have been identified by a combination of physical values of SWIR, visible albedo and TIR1 BT (red colour clusters marked with fog pixels). It is also seen that TIR1 BT between 270 and 290 K,

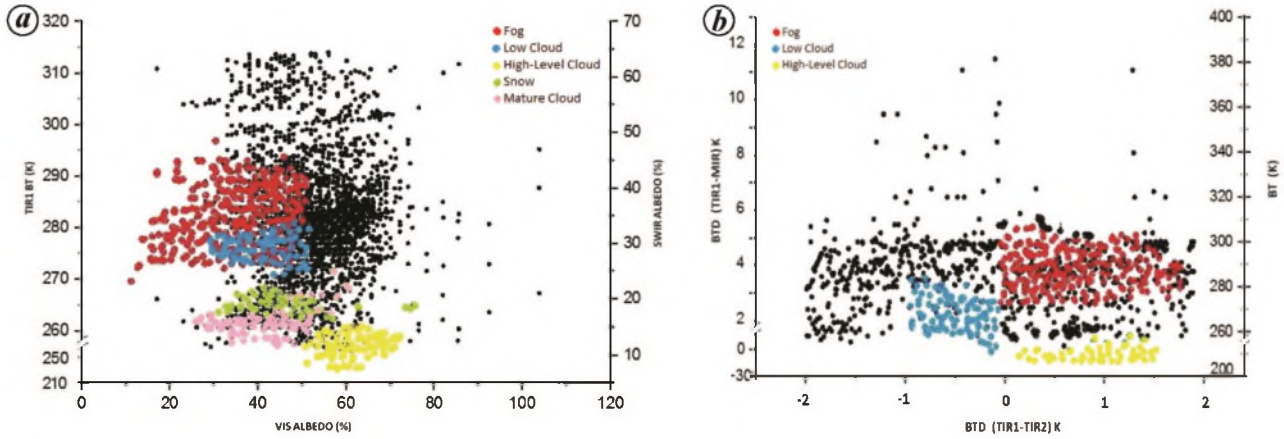

Figure 3. Scatter plot of (*a*) DMP (*b*) NMP of different clusters including non-concurrent data shown in black.

Table 3. Day microphysics (DMP) and night microphysics (NMP) thresholds along with resolution and time of use for fog and low clouds

Product	Resolution (km)	Time	Source	Use (conditions)
Night-time RGB (3.9, 10.8 μm)	1–4	13 to 02 UTC (of next day)	RAPID (rapid.imd.gov.in)	1. TIR2–TIR1 BT DIFF > must be +1 to –1 K 2. TIR1–MIR BT >2.5 K 3. TIR1 BT >279 K ⇒ fog
		Half hourly		1. TIR2–TIR1 BT DIFF> –1 to 0 K 2. TIR1–MIR BT >2.5 K 3. TIR1 BT <275 K ⇒Low cloud/mist/haze
Day-time RGB	1–4	02 : 30 to 12 : 30 UTC Half hourly	RAPID (rapid.imd.gov.in)	TIR1 BT between 255–275 K and VIS 30–45%, and SWIR 31–60% ⇒ low cloud TIR between 276–290 K and VIS 16–55% and SWIR 31–60% ⇒ fog

SWIR values between 31% and 60% and visible values between 16% and 55% correspond to fog pixels, whereas pixels with blue colour in scatter plot having TIR1 BT between 255 and 275 K, SWIR values ranging from 31% to 60% and visible values ranging from 30% to 45% identified as low clouds. It can be seen from the scatter plot that the threshold difference (SWIR and VIS) between low clouds and fog is not high as only thermal BT is the main parameter to be considered. Similarly, TIR1 BT <255 K, VIS albedo >50% and SWIR albedo <25% correspond to the high-level clouds (CB cell, yellow colour in scatter plot). For snow pixels (green colour in scatter plot), VIS albedo > 35%, TIR1 BT between 260 and 280 K and SWIR albedo <20% and for mature clouds (pink colour in scatter plot), VIS albedo lies between 30% and 50%, TIR1 BT value <260 K and SWIR albedo <40%. The DMP RGB is useful as far as classification of cloud types, convection, fog and the location of snow area are concerned. In this colour scheme water clouds that do not precipitate appear white because cloud drops are small, whereas large drops that are typical to precipitating clouds appear pink because of the low reflectance at 3.9 μm channel[10].

From Figure 3 *b* pixels with red colour in the scatter plot, it is seen that for BT >279 K, BT difference of TIR1–MIR >2.5 K and BT difference of TIR1–TIR2 between 0 to 2 K correspond to fog pixels, whereas pixels with blue colour in scatter plot having BT value between 250 and 265 K, BT difference of TIR1–MIR value >4 K and BTD TIR1–TIR2 between 0 and –1 K correspond to low clouds. This is just because over the land region, if low clouds and fog where the BT is more than 279 K, the difference becomes positive. This situation occurred during temperature inversion. Similarly, for CB cell (yellow colour in scatter plot), the threshold suggesting a pixel of BT <245 K, BT difference of TIR1–MIR value <–30 K and BT difference TIR1–TIR2 value is in the range of 0 to 1.5 K. Based on the information given in Figure 3, the checklist thresholds for identification of fog have been computed. However, sometimes fog/low clouds are not identified during the surface observations due to their small horizontal dimensions. Therefore, the detection of fog or clouds using this scheme of thresholds is completely objective as well as dynamic in nature. The thresholds are prepared for both, night and daytime microphysics. Table 3 lists the DMP and NMP thresholds

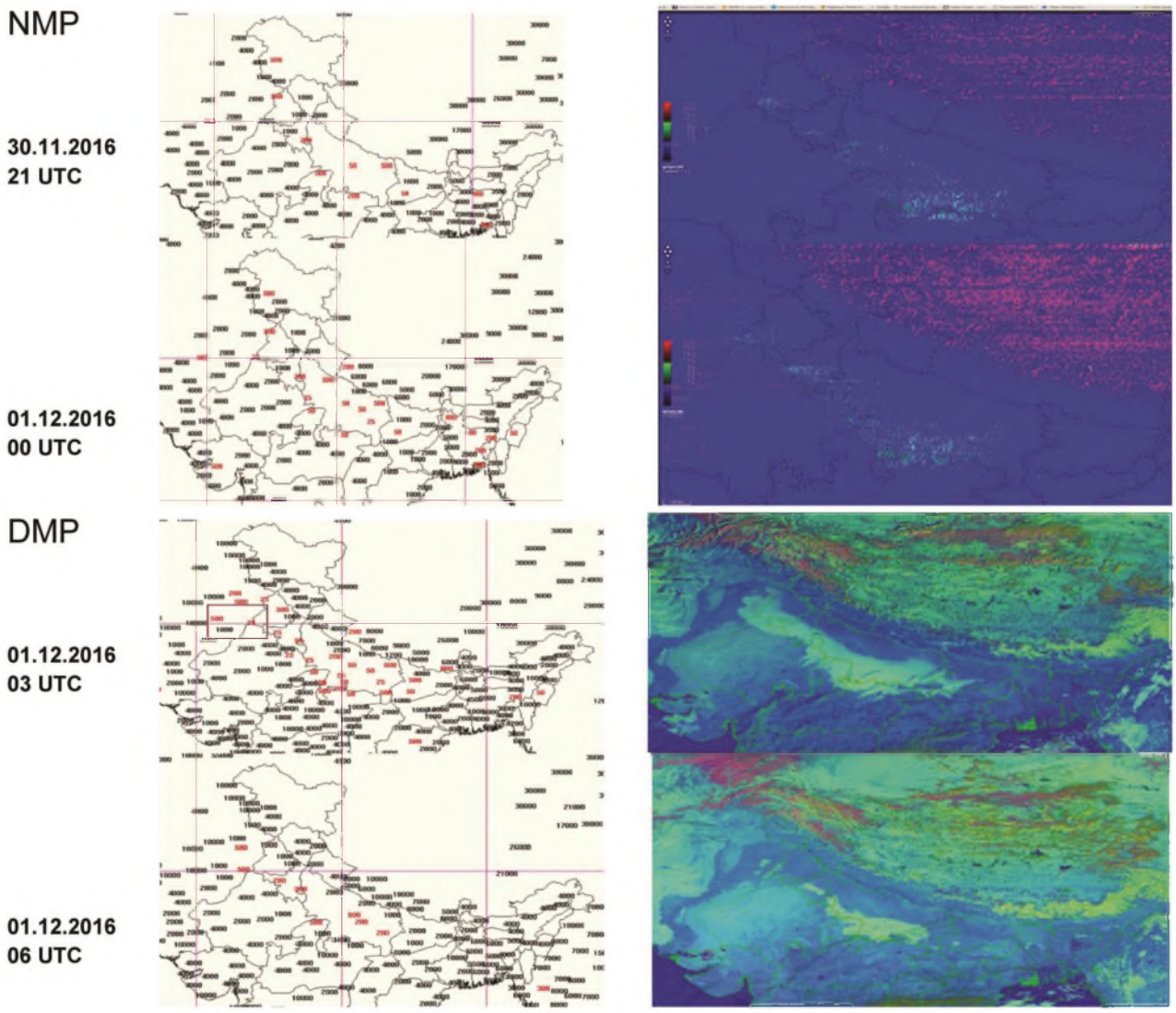

Figure 4. Spatial distribution of DMP and NMP fog with actual visibility observations on 30 November and 1 December 2016. The red colour represent the visibility less than 1000, 500, 200 and 50 m.

along with their resolution and time of use for identification of fog and low clouds.

Based on the threshold criteria of Table 3, the occurrence of fog is compared with three-hourly *in situ* visibility data from IMD observatories. The day and night-time microphysics RGB images are spatially compared with visibility chart on 30 November and 1 December 2016 (Figure 4). The visibility data less than 500 km are shown in red colour in the chart. It can be seen from the figure, that the spatial coverage of NMP fog areas (shown in white) fully matches with visibility data chart over the southern parts of Uttar Pradesh and Northern Madhya Pradesh during 30 November, 21 UTC to 1 December 2016, 00 UTC. Similar spatial map of DMP fog shows good agreement with the *in situ* visibility observation on 1 December 2016 at 03 and 06 UTC.

Data from MODIS, a key instrument aboard the Terra and Aqua satellites, have been taken from NASA's tool called Earth Observing System Data and Information System (EOSDIS), which provides the capability to interactively browse global, full-resolution satellite imagery and then download the underlying data. An intense fog layer is prevalent over the Indo-Gangetic Plains as can be seen in Figure 5, which is shown as a thick mass of white patch (yellow circle). From Figure 5 *a*, it can be seen that fog was initiated in the foothill of the Himalaya and it gradually extended spatially and covered Bihar and parts of north Uttar Pradesh. The spatial extent continued to increase both from east to west as well as in the southern direction starting from the foothills of the Himalaya to south Uttar Pradesh (Figure 5 *b*). In the beginning of January, local moisture availability and the temperature inversion in the north Madhya Pradesh and southern parts

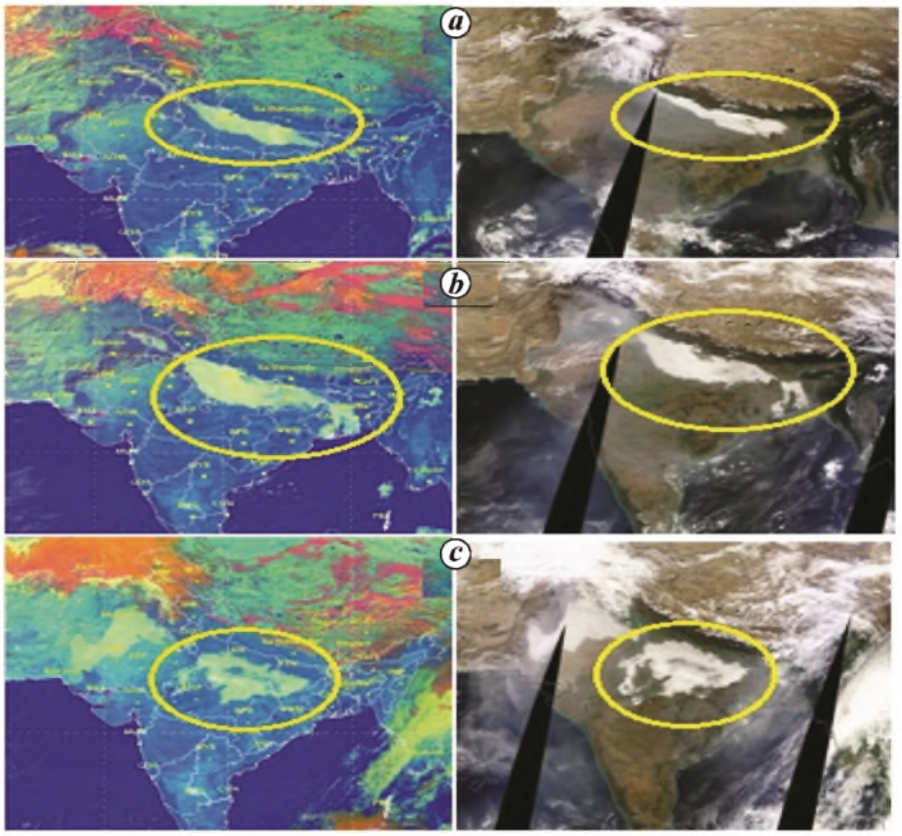

Figure 5. Comparison of MODIS fog map (yellow circles) with DMP fog having less than 500 km visibility on (*a*) 16 December 2016, (*b*) 28 December 2016 and (*c*) 3 January 2017.

Table 4. Contingency table illustrating the counts used in verification statistics for dichotomous (e.g. yes/no) INSAT-3D RGB (DMP/NMP) and observations

	Observed (visibility, three-hourly)	
INSAT-3D RGB (DMP/NMP)	Yes	No
Yes	Hits (YY)	False alarms/detection (YN)
No	Misses (NY)	Correct rejections (NN)
	YY + NY	YN + NN

Critical success index (CSI) = Hits/(hits + misses + false alarms) [range: 0 to 100%; 0 indicates no skill; perfect score: 100%]. Probability of detection (POD) = Hits/hits + misses [range: 0 to 100%; 0 indicates no skill; Perfect score: 100%]. FAR = False alarm/hits + false alarm.

of Uttar Pradesh developed in the early hours of the day (Figure 5 *c*). The gradient in the fog map shows that the intensity of fog is between dense to very dense, i.e. the *in situ* visibility is less than 500 m for all the three images. The DMP product has captured almost the same area of fog coverage, as is observed in the MODIS fog observations. The qualitative inter-comparison of the two maps as shown in Figure 5 *a–c* indicates good agreement with each other. A quantitative validation of threshold technique has been carried out against the *in situ* visibility data for northern and northeastern parts of India from December 2015 to February 2016 and December 2016 to February 2017 for both, DMP and NMP products (Table 5). Overall 180 days of three-hourly *in situ* visibility observations with 720–720 number of samples in DMP and NMP have been considered. A statistically description in the form of contingency table of the verification of INSAT-3D RGB with actual observation is given in Table 4.

Table 5 shows that the POD using DMP threshold is 94%, however, due to the presence of low clouds, the FAR was 8% and number of miss was 9. This usually encountered when horizontal visibility at the surface level is the high, but spectral behaviour of the channels is almost similar. The BT difference for low clouds is also high like fog.

Table 5. Statistics of daytime and night-time fog detection using threshold criteria

Indices	DMP	NMP
Total no. of observations (days)	180	180
Number of hits (visibility (m), 50, 200, 500)	157	140
Number of misses	9	23
Number of false detection	14	17
Probability of detection (POD)	94%	85%
Critical success index	87%	77%
False alarm ratio (FAR)	8%	10%

From Table 5, the POD using NMP threshold is 85%, however, the higher false detection compared to DMP is due to the presence of low clouds. During the winter nights, northerly cold winds prevails over the northern, northwestern regions, which carry high clouds followed by the advection fog. Sometimes these high clouds with fog restrict threshold to capture the phenomenon. This technique is useful for operational weather forecasters to enhance specific features such as low/medium clouds, fog, snow, etc. Compared with other methods, these RGB thresholds help analyse weather, both using qualitatively as well as quantitatively. The probability of detection of fog showed improvement compared to earlier findings of Mitra *et al.*[4] and Sasmita *et al.*[2]. In the earlier study, Sasmita *et al.*[17] had reported using a bi-spectral threshold technique, during the day-time, the accuracy of fog identification is limited due to similar spectral behaviour of snow, fog and other water clouds in the visible bands and the contamination of the 3.9 μm band by solar radiation[16]. Small fog droplets reflect at this wavelength. In these situations, daytime and night-time RGBs have some advantages. For the best utilization of INSAT-3D RGBs, it must be ensured that RGB products are developed with a defined recipe and that each product is well adapted to its utilization so that forecasters comprehend what they are taking at in a given RGB product. The World Meteorological Organization adopted these RGB best practices to develop a set of standard products among international partners[7]. Since RGBs are intended to upgrade a particular phenomenon, to detect particular features, spectral bands or differences between pairs of bands are specifically chosen. Prior to the INSAT-3D observations, detection of low cloud, snow, convection and night-time fog was difficult. Now, these RGB recipes (Figure 3 *b*) incorporate the well-known ΔBT between 11 μm and 3.9 μm. The difference in the intensity of the LWIR- and SWIR at these two wavelengths used to differentiate between water and ice clouds. The 12 and 11 μm ΔBT helps distinguish between high, thick clouds and high, thin clouds by delineating cloud phase (ice or liquid water) and cloud particle size (small or large). The IR brightness temperature is mainly included to enhance low, warm clouds and distinguish them from colder, higher clouds.

At present the DMP and NMP scheme being applied only on Imager payload at IMDPS. In DMP, water and ice cloud which is more sensitive to the different cloud microstructure, sometime lacks valuable information of cloud top temperature and thus reduces the delectability of thin clouds. In the orographic region, the development of CB cell sometimes gives rise to false alarms because of rising air motion originating at a high level (can be called orographic wave clouds) from the surface and misleading in the NMP. The Lensky and Rosenfeld[10] technique is basically applied on rich spectral information of Spinning Enhanced Visible and Infrared Imager (SEVIRI) on-board METEOSAT Second Generation (MSG, 11 bands spectral information) – the European geostationary satellite operated by EUMETSAT, which has multispectral capability for cloud microphysical characterization and aerosol–cloud interaction detection. In the current INSAT-3D channels, we have used six-band spectral information imager. In the RAPID tool, the large reflectance of the CB cell and lower level clouds is sometimes not detectable because of unavailability of 0.8 and 1.6 μm in the DMP colour scheme. The difference between 1.6 and 0.6 μm of solar reflectance plays a major role in discriminating the ice clouds and surface. The large negative difference between 1.6 and 0.6 μm indicates ice clouds, and a much larger positive difference between 1.6 and 0.6 μm is typical for the surface. Another missing channel in the INSAT-3D satellite is the 8.7 μm channel, which is most sensitive to clouds particle effective radius in the night. This particular channel can also be used in sand and dust discrimination. The RGB scheme has also some limitations during dawn to dusk period.

The daytime and night-time RGB scheme is presented here using RAPID visualization tool for INSAT-3D satellite data on real-time basis for identification of weather events. The thresholds technique has been developed separately for both the RGB products with two years of data for the identification of fog, snow and low clouds. The quantitative validation of these thresholds has been carried for fog and different types of clouds during 2015–16 and 2016–17 of December to February and spatially coverage areas from MODIS data. It has been found that the RGBs, i.e. DMP and NMP have reasonable agreement with ground-based observations and MODIS data. This threshold technique yields a good probability of fog detection more than 94% and 85% with acceptable false alarm conditions less than 8% and 10% for DMP and NMP respectively. The technique has significantly minimized the misclassification between low clouds, snow and fog. The threshold technique is found to be useful for day-to-day weather forecasting and is being used by forecasters and the user community. Work is in progress to apply the DMP and NMP colour scheme over the 19 channels of INSAT-3D Sounder and thereafter the newly launched INSAT-3DR satellite, so that staggering of both the satellites will provide us information every 15 min of weather events over the Indian region. Further refinement

of these products in the perspective of the upcoming GEO Imaging Satellite (GISAT) missions is also being planned. GISAT is an Indian geo-imaging satellite for providing images quickly during disasters.

1. Gultepe, I. *et al.*, The fog remote sensing and modelling (FRAM) field project and preliminary report. *Bull. Am. Meteorol. Soc.*, 2009, **90**(3), 341–359.
2. Chaurasia, S. and Gohil, B. S., An objective method for detecting night time fog using MODIS data over northern India. *J. Geomat.*, 2016, **10**.
3. Tiwari, S., Payra, S., Mohan, M., Verma, S. and Bhisht, D. S., Visibility degradation during foggy period due to anthropogenic urban aerosol at Delhi, India. *Atmos. Pollut. Res.*, 2011, **2**, 116–120.
4. Mitra, A. K., Sankar Nath and Sharma, A. K., Fog forecasting using rule-based fuzzy inference system. *J. Indian Soc. Remote Sensing*, 2008, **36**(3), 243.
5. Roy Bhowmik, S. K., Sud, A. M. and Singh, C., Forecasting fog over Delhi – an objective method. *MAUSAM-55*, 2004, **2**, 313, 322.
6. Brij Bhusan, Trivedi, H. K. and Bhatia, R. C., On the persistence of fog over northern parts of India. *MAUSAM-54*, 2003, **4**, 851–860.
7. Berndt, E. B., Molthan, A. L., Vaughan, W. W. and Fuell, K. K., Transforming satellite data into weather forecasts. *AGU EOS*, 2017, **98**; https://doi.org/10.1029/2017EO064449.
8. Lensky, I. M. and Rosenfeld, D., Clouds-Aerosols-Precipitation Satellite Analysis Tool (CAPSAT). *Atmos. Chem. Phys.*, 2008, **8**, 6739–6753.
9. Inoue, T., An instantaneous delineation of convective rainfall areas using split window data of NOAA-7 AVHRR. *J. Meteor. Soc. Jpn*, 1987, **65**, 469–481.
10. Lensky, I. M. and Rosenfeld, D., Satellite-based insights into precipitation formation processes in continental and maritime convective clouds at nighttime. *J. Appl. Meteor.*, 2003, **42**, 1227–1233.
11. Lensky, I. M. and Rosenfeld, D., A night rain delineation algorithm for infrared satellite data based on microphysical considerations. *J. Appl. Meteor.*, 2003, **42**, 1218–1226.
12. Eyre, J. R., Brownscombe, J. L. and Allam, R. J., Detection of fog at night using advanced very high resolution radiometer. *Meteorol. Mag.*, 1984, **113**, 266–271.
13. Bader, M. J., Forbes, G. S., Grant, J. R., Lilly, R. B. E. and Waters, J., *Images in Weather Forecasting*, Cambridge University Press, 1995, p. 493.
14. Ellord, G. P., Advances in the detection and analysis of fog at night using GOES multi spectral infrared imagery. *Weather Forecasting*, 1995, **10**, 606–619.
15. Bendix, J., A satellite-based climatology of fog and low-level stratus in Germany and adjacent areas. *Atmos. Res.*, 2002, **64**, 3–18.
16. Bendix, J. and Bachmann, M., A method for detection of fog using AVHRR-imagery of NOAA satellites suitable for operational purposes. *Meteorol. Rund.*, 1991, **43**, 169–178 (in German).
17. Chaurasia, S., Sathiyamoorthy, V., Paul Shukla, B., Simon, B., Joshi, P. C. and Pal, P. K., Night time fog detection using MODIS data over Northern India. *Meteorol. Appl.*, 2011, **8**(4), 483–494.

ACKNOWLEDGMENTS. We thank the Space Applications Center, Ahmedabad team for their technical, software expertise and implementation of RAPID tool at IMDPS, New Delhi. We specially thank C. M. Kistawal, Shri Ghansyam Sanger and Nitesh Kausik for their valuable suggestions while developing 'RAPID'. The first author thanks to I. M. Lensky and D. Rosenfeld for CAPSAT tool information. We appreciate the assistance of the following persons during the course of research: Mr Virendra Singh and S. K. Mukerjee, IMD for data recovery.

Received 21 December 2017; revised accepted 26 March 2018

doi: 10.18520/cs/v115/i7/1358-1366

Analysis of WorldView-2 band importance in tree species classification based on recursive feature elimination

Huaipeng Liu[1,*], Huijun An[2] and Yongxin Zhang[1]

[1]School of Land and Tourism, Luoyang Normal University, Luoyang, Henan Province, 471934, China
[2]College of forestry, Inner Mongolia Agricultural University, Huhhot, Inner Mongolia, 010019, China

In tree species classifications, different spectral bands feature different importance, and the manner of determining the importance of one band is a problem that needs to be solved. In this study, eight bands of the WorldView-2 fusion data were used as information sources, and a recursive feature elimination based on maximum likelihood (MLC-RFE) was used to sort the importance of these bands. According to the results, the importance of the eight bands was sorted as follows (from important to unimportant): near-infrared 2 > red edge > yellow > red > near-infrared 1 > coastal blue > green > blue. The poorest band combination yielded the lowest overall accuracy (OA) and Kappa coefficient (40.9153%; 0.3080), whereas the optimal band combination presented the highest OA and Kappa coefficient (74.5479%; 0.7029), indicating the large difference in accuracies between the optimal and poorest band combinations. Therefore, selecting important bands bears significance in tree species classifications. The MLC-RFE method significantly solved the band selection problem. Thus, this method should be extended to more complex feature selections.

Keywords: Bands importance, maximum likelihood, recursive feature elimination, tree classification, WorldView-2.

TREE species classification based on image remains an unsolved problem, and it is also a hot topic causing concern in researchers[1,2]. Thus far, numerous scholars consider WorldView-2 or WorldView-2 combined with IKONOS, Quickbird, Lidar and other data as data sources to classify tree species. They use classifiers of decision trees, random forests, linear discriminant analysis, partial least squares discriminant analysis, maximum likelihood and support vector machines to distinguish native tree species and other ground types. The overall accuracy (OA) of these classification results is between 82% and 94%, indicating that related studies have acquired better results[3–11]. However, given the lack of sufficient spectral information, mapping forest types and tree species using

*For correspondence. (e-mail: gatestudy@163.com)